arXiv:1003.5387v1 [cond-mat.mes-hall] 28 Mar 2010

Conserved spin and orbital phase along carbon nanotubes connected with multiple ferromagnetic contacts

C. Feuillet-Palma[1,2], T. Delattre[1,2], P. Morfin[1,2], J.-M. Berroir[1,2], G. Fève[1,2], D.C. Glattli[1,2,3],B. Plaçais[1,2], A. Cottet[1,2] and T. Kontos[1,2*]
[1] *Ecole Normale Supérieure, Laboratoire Pierre Aigrain, 24, rue Lhomond, 75231 Paris Cedex 05, France*
[2] *CNRS UMR 8551, Laboratoire associé aux universités Pierre et Marie Curie et Denis Diderot, France*
[3] *Service de physique de l'état Condensé, CEA, 91192 Gif-sur-Yvette, France.*
(Dated: March 30, 2010)

We report on spin dependent transport measurements in carbon nanotubes based multi-terminal circuits. We observe a gate-controlled spin signal in non-local voltages and an anomalous conductance spin signal, which reveal that both the spin and the orbital phase can be conserved along carbon nanotubes with multiple ferromagnetic contacts. This paves the way for spintronics devices exploiting both these quantum mechanical degrees of freedom on the same footing.

PACS numbers: 73.23.-b,73.63.Fg

I. INTRODUCTION

The scattering imbalance between up and down spins at the interface between a non-magnetic metal and a ferromagnetic metal is at the heart of the principle of the magnetic tunnel junctions or multilayers celebrated in the field of spintronics[1,2]. Although these devices use the quantum mechanical spin degree of freedom and electron tunneling, they do not exploit a crucial degree of freedom involved in quantum mechanics: the phase of the electronic wave function. In most of the devices studied so far, this aspect has not been developed owing to the classical-like motion of charge carriers in the conductors used[3].

Quantum wires or molecules have emerged recently as a promising means to convey spin information[4–11]. In these systems, the electronic gas is confined in two or three directions in space, making quantum effects *a priori* prominent. In this context, most of the studies have been carried out in two terminal devices, i.e. with two ferromagnetic contacts. The need for integration and more complex architectures for manipulating spin information[12–16] brings on the question of what happens when a spin active nanoscale conductor is connected to more than two reservoirs. Multi-terminal transport has been central in (spin independent) mesoscopic physics, in particular with the observation of non-local electric signals due to the delocalization of electronic wave functions[17–19]. Can this quantum mechanical nonlocality survive and ultimately be exploited in spintronics devices combining nanoscale conductors and ferromagnets ?

In this article, we address this question through multi-terminal spin dependent transport measurements in single wall carbon nanotubes (SWNTs) with ferromagnetic and non-magnetic contacts. Non-local voltage and conductance measurements reveal that the spin as well as the orbital phase are conserved along the whole active part of our SWNTs. We observe a *non-local spin field effect transistor*-like action which is a natural consequence of quantum interference in a few channel conductor. In spite of the inherent complexity of the spectrum of our devices, we can account well for our findings using a simple theory based on a scattering approach. These results bridge between mesoscopic physics and spintronics. They open an avenue for nanospintronics devices exploiting both the spin and the orbital phase degrees of

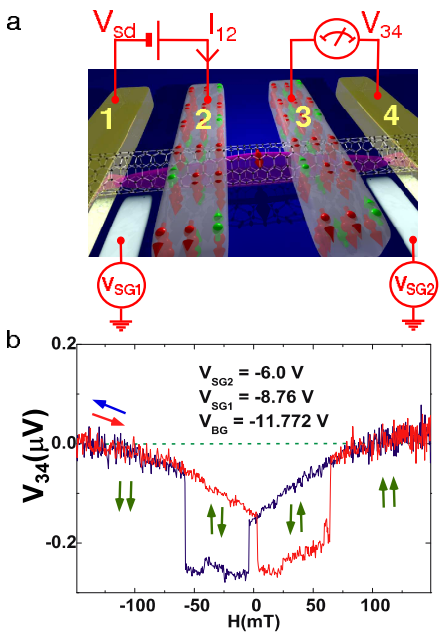


FIG. 1: **a.** Schematics diagram of the devices studied in the article. **b.** Non-local voltage V_{34} for sample I as a function of the external magnetic field H for side gate voltages $V_{SG1} = -8.76V$, $V_{SG2} = -6.00V$ and a back gate voltage $V_{BG} = -11.772V$.

*To whom correspondence should be addressed: kontos@lpa.ens.fr

freedom, which could provide new means to manipulate the electronic spin, because the orbital phase of the carriers can easily be coupled to the local electric field in nanoscale conductors.

The principle of non-local transport measurements is to use a multi-terminal structure with two terminals playing the roles of source and drain, and the others the role of non-local voltage probes. Since the pioneering work by Johnson and Silsbee in metals[20], non-local spin dependent voltages have been studied in various multichannel diffusive circuits based on semiconducting heterostructures[21], metallic islands[22] and graphene[23]. These signals are well captured using a *classical* bipartite resistors network, with two branches corresponding to opposite spin directions[24]. The non-local spin signal stems from the imbalance between the up spin and down spin branches of the network, which reflects the imbalances between e.g. the two spin populations. Importantly, this interpretation is valid only when one can neglect quantum mechanical non-local signals which arise from the delocalization of the carrier's wave function.

Coherence effects induce only corrections to transport at low temperatures in metals or semiconducting heterostructures which involve many conducting channels[25]. In contrast, coherence becomes essential in understanding transport in molecules or quantum wires where quantum mechanics primarily controls conduction. The studies of non-local spin transport in the coherent regime have been elusive so far. Here, we use the high versatility of Single Wall carbon NanoTubes (SWNT) to achieve the required devices and to explore these phenomena. We observe a gate-controlled spin signal in non-local voltages and an anomalous spin conductance which are specific to the coherent regime.

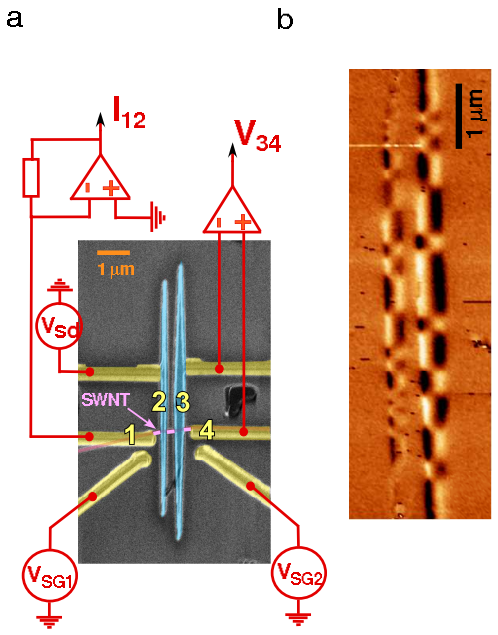


FIG. 2:
a. SEM picture of sample I. The NiPd electrodes are highlighted in blue and the Pd stripes are highlighted in yellow. The SWNT is highlighted in purple. The orange scale bar is $1\mu m$. **b.** MFM characterization of the NiPd electrodes at room temperature on a test device similar to sample I without the SWNT. The black scale bar is $1\mu m$.

II. EXPERIMENTAL SETUP

We use the measurement scheme represented on figure 1a. Our devices are made out of a SWNT connected to 4 electrodes labelled 1,2,3 and 4 from the left to the right, with 2 and 3 ferromagnetic $NiPd$ electrodes and 1 and 4 non-magnetic Pd electrodes. In addition, the device is capacitively coupled to a back-gate electrode with voltage V_{BG} and two side gate electrodes with respective voltages V_{SG1} and V_{SG2}, acting mainly on sections 12 and 34 of the nanotube respectively. Throughout the paper, the temperature is set to $4.2K$.

A SEM picture of a typical device is shown in figure 2a. We use chemical vapor deposition with a standard methane process to fabricate our SWNTs on a Si substrate. We localize the SWNTs with respect to Au alignment markers by Scanning Electron Microscopy (SEM) or Atomic Force Microscopy (AFM). We fabricate the contacts and gates using standard e-beam lithography and thin film deposition techniques. We deposit the normal and the ferromagnetic contacts in one fabrication step using shadow evaporation techniques. The central ferromagnetic electrodes consist of a 30nm-thick $Ni_{0.75}Pd_{0.25}$ layer below a 70nm-thick Pd layer. The normal contacts consist of 70nm of Pd. Such a method allows to achieve two probe resistances as low as 30kOhm between the normal and the ferromagnetic reservoirs. In addition to the highly doped Si substrate with $500nm$ SiO_2 which is used as a global backgate, we fabricate two side gates whose voltages V_{SG1} and V_{SG2} are used to modulate transport in our devices. Each nanotube section defined in this manner has a length ranging from $300nm$ to about $600nm$.

Our measurements are carried out applying an AC bias voltage V_{sd} of about 200 to $300\mu V$ between the normal electrode 1 and the ferromagnetic electrode 2, at a typical frequency of $77.7Hz$. This generates a finite non local voltage V_{34} between the ferromagnetic electrode 3 and the normal electrode 4. We also measure simultaneously the conductance $G = dI_{12}/dV_{sd}$. Note that a finite V_{34} has already been observed in similar but non-magnetic devices due to coherent propagation of electrons in the SWNT and lifting of the K/K' degeneracy[19]. Here, we focus on the specific effects due to ferromagnetic leads. A spin contrast is obtained by comparing the electric signals in the parallel (P) configuration (magnetizations of electrodes 2 and 3 pointing in the same direction) and in the (AP) configuration (magnetizations pointing in opposite directions). A finite magnetic field is applied in plane parallel to the easy axis of the ferromagnetic

electrodes (for samples I and III), which is transverse as shown by MFM characterization carried out at room temperature (see figure 2b). The observed magnetic contrast shows the presence of large transverse domains of a typical size of $1\mu m$. Due to the different widths of respectively $150nm$ and $250nm$, the coercive fields of the two ferromagnetic electrodes are different. Generally, this leads to a sharp switching at about $50mT$ for one of the electrodes. For the lower field switching, it turns out to be more difficult to obtain systematically switchings as sharp as those of sample I. The P and AP configuration can be obtained selectively by sweeping the external magnetic field. We determine $MV = V_{34}^P - V_{34}^{AP}$ and $MG = 100(1 - G^{AP}/G^P)$.

III. GATE CONTROLLED NON-LOCAL SPIN SIGNAL.

The magnetic field dependence of the non-local voltage V_{34} of sample I is shown in figure 1b. Upon increase and decrease of the external magnetic field H, the characteristic hysteretic switching of a spin valve is observed. We observe sharp switchings which show that the external field is well aligned with the magnetic anisotropy of both electrodes in this case. Upon increasing H (see red line in figure 1b), we obtain the AP configuration for $H \in [10mT; 50mT]$, and the P configuration otherwise. For the particular gate voltage set used in figure 1b, V_{34} changes from $V_{34}^P = -0.12\mu V$ to $V_{34}^{AP} = -0.25\mu V$ upon switching from the P to the AP configuration, leading to a finite MV. Unlike the majority of our samples, this spin signal is superimposed to an intrinsic background here (see discussion in section IV). A finite MV has already reported in multichannel incoherent diffusive conductors[21,22,26]. One of the main results of the present work is the observation of a *gate control* of MV, as a consequence of quantum interferences, which contrasts with these previous works. Such a fact not only sheds light on the peculiar nature of spin injection in coherent few channel conductors, but also allows to rule out non-spin injection effects related to stray fields for example as we will see in section IV.

As soon as a metallic electrode is deposited on the top of a SWNT, a scattering region is created below the contact, which partially decouples the two sides of the nanotube defined by the electrode. The multi-dot nature of our devices appears on figure 3a, where V_{34}^P is represented in a greyscale plot as a function of V_{SG1} and V_{SG2} for sample I. We observe white horizontal and vertical stripes, rather regularly spaced, which correspond to negative anti-resonances in V_{34}^P. Such a "tartan" pattern is very much alike the stability diagram of a double quantum dot in the electrostatically decoupled regime[28]. The stripes correspond to discrete energy levels "engineered" by defining the 3 different sections of the nanotube with the 4 electrodes. The fact that horizontal as well as vertical stripes are observed shows that the side gate electrodes control essentially independently different parts of the device, which carry different energy levels. Our devices can be seen as a series of three Fabry-Perot electronic interferometers with local gate control. The nature of the coupling between these interferometers is a crucial question for the development of orbitally phase coherent spintronics.

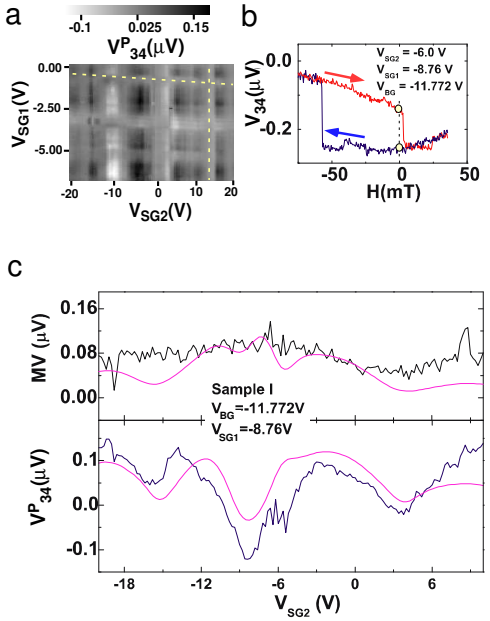


FIG. 3: **a.** Greyscale plot showing the "tartan" pattern of the non local voltage V_{34}^P of sample I in the P configuration. **b.** "Minor hysteresis loop" for the non-local voltage V_{34} of sample I for $V_{SG1} = -8.76V$, $V_{SG2} = -6.00V$ and $V_{BG} = -11.772V$. **c.** V_{34}^P and MV as a function of V_{SG2}. In purple, the prediction from the multi-terminal scattering theory of ref. 27 with the parameters described in the appendix.

One can measure the spin signals by placing the system in the remanent state of magnetization either in the P or in the AP configuration (for samples with a sufficiently high stability). This is done by imposing to the device a "minor loop" which is represented in figure 3b. In such a cycle, the magnetic field is swept in such a way as to reverse selectively one magnetization without reversing the other. Depending on how the external field is swept back to zero, one can reach either the P or the AP configuration. Then, for each of these configurations, we measure in a single shot the gate dependence of V_{34}. This method has been used to obtain MV in figure 2c. The existence of quasi bound-states inside the nanotube induces variations of both V_{34} and MV as a function of the gate voltages. This effect can be observed when V_{SG2} is swept, V_{SG1} being kept constant, for example (see fig. 3c). The interference fringes observed correspond to the "tartan" pattern of figure 3a. For $V_{SG1} = -8.76V$ and $V_{BG} = -11.772V$, V_{34}^P and V_{34}^{AP} evolve almost in parallel as a function of V_{SG2}. This results in a weakly gate dependent MV with a constant positive sign as shown

in figure 3c. We find that V_{34}^P and V_{34}^{AP} can be of opposite sign, as well as of the same sign depending on the values of V_{SG2} and V_{SG1}. In carbon nanotubes, this phenomenon originates both from transverse and longitudinal size quantization.

In the spectroscopy of our devices, Coulomb blockade effects are generally absent (see e.g. Fig. 6b). This motivates a comparison between our data and the non-interacting scattering model of ref. 27 (see appendix for details). This model uses four scattering channels, to account for the up/down spins and the K and K' orbitals of carbon nanotubes. For simplicity, we assume that the spin and K/K' degrees of freedom are conserved along the whole device. Between two consecutive contacts $i \in \{1,2,3\}$ and $j = i+1$, electrons acquire a "winding" quantum mechanical phase δ_{ij}. The effect of each metal/nanotube contact is described with a scattering matrix which depends on the contact transmission probability. In the case of a ferromagnetic contact, we also take into account the spin-polarisation of the transmission probabilities and the Spin Dependence of Interfacial Phase Shifts[29,30]. This scattering model is fully coherent, i.e. the phase of the electronic wave function is conserved even when electrons pass in the nanotube sections below the ferromagnetic contacts 2 and 3. The results of the scattering theory of ref. 27, shown in magenta in figure 3c, are in qualitative agreement with our data. The variations of V_{34}^P are well accounted for as well as the sign and the order of magnitude of MV. Importantly, the coherent model of ref. 27 involves resonance loops which are extended on several sections of the nanotube, e.g. between leads 1 and 3.

The gate modulations of V_{34}^P as well as the gate dependence of MV is a natural consequence of delocalization of the electronic wave function in our devices. Similarly to optics, the multiple reflections at the contacts give rise to (electronic) interference which lead to gate modulations of the physical signals. It is important to note that the origin of this gate modulation is not related to the spin-orbit interaction which lead to energy splittings of the order of $0.4meV$ in SWNTs[31]. This fact will become even clearer in section V where we identify the energy scale responsible of the modulations as the single particle level spacing of one of the NT section (namely section 12). Finally, it is important to note that here, contrary to the multichannel diffusive case, coherence naturally couples the spin and the charge of carriers. Therefore, a non-local measurement does not "separate spin and charge transport" as is often stated[11] in the coherent few channel case. Rather, it gives a new path for manipulating spin information with electric fields at low temperature.

IV. BACKGROUND MAGNETORESISTANCE AND STRAY FIELD EFFECTS

As one can see in figure 1b, there is a finite background for the non-local voltage as a function of the magnetic field, superimposed to the hysteresis. This might question the effect of the stray fields on the observed signals. Note, however, that no background is observed in figure 5a and c, a behavior which is common to the majority of our samples. This makes the device essentially insensitive to stray fields for the majority of samples studied. In order to rule out the stray field effects for sample I, we present in figure 4 hysteresis loops for two of the different gate voltages, namely $V_{SG2} = -6.0V$ and $V_{SG2} = -2.65V$. The curves for $V_{SG2} = -2.65V$ have been shifted up to make them coincide with those for $V_{SG2} = -6.0V$ at zero field. As one can see on this figure, while the backgrounds are almost exactly the same (up to small gate shifts), the MV's clearly differ. Therefore, the observed gate dependence of the MV for sample I cannot be attributed to stray field effects.

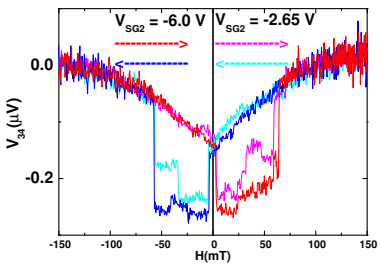


FIG. 4:
Non-local voltage V_{34} for sample I as a function of the external magnetic field H for $V_{SG2} = -6.0V$ and $-2.65V$. The curves for $V_{SG2} = -2.65V$ has been shifted up to make them coincide with those for $V_{SG2} = -6.0V$ at zero field.

V. ANOMALOUS NON-LOCAL MAGNETORESISTANCE

In the multichannel diffusive incoherent regime, a hysteretic *non-local voltage* can arise, but one can show that the *intrinsic locality of charge transport* makes it very difficult for the conductance $G = dI_{12}/dV_{sd}$ to depend on the relative magnetic configuration of the ferromagnetic electrodes[3,32]. This contrasts with our devices as shown in fig. 5b and d where $MG \neq 0$ is obtained. In order to show that the spin signals observed in G and V_{34} arise from a property of the device as a whole, it is crucial to measure G and V_{34} simultaneously. In figure 5a and b (resp. 5c and d), the magnetic field dependences of the non-local voltage and the conductance of sample II (resp. III) are shown for different gate voltages. A hysteresis is observed simultaneously for both quantities upon cycling the magnetic field. For the measurements of figure 5a and b, contrarily to the two other samples presented in this article, the external magnetic field has been applied in plane, *perpendicular to the magnetic anisotropy* of the ferromagnetic electrodes. In such a situation, the motion of the magnetic domains often displays a complex behav-

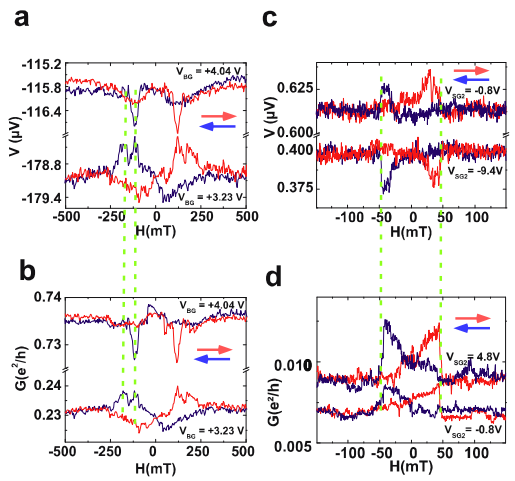


FIG. 5: **a.** Non-local voltage V_{34} for sample II as a function of the external magnetic field H for $V_{SG1} = 0.00V$, $V_{SG2} = 0.00V$ and $V_{BG} = 4.04V$ or $V_{BG} = 3.23V$. **b.** Similar plot for G of sample II. **c.** Non-local voltage V_{34} for sample III as a function of H for $V_{SG1} = -5.00V$, $V_{BG} = -5.455V$ and $V_{SG2} = -9.4V$ or $V_{SG2} = -0.8V$. **d.** Similar plot for G of sample III for $V_{SG1} = -5.00V$, $V_{BG} = -5.455V$ and $V_{SG2} = 4.8V$ or $V_{SG2} = -0.8V$.

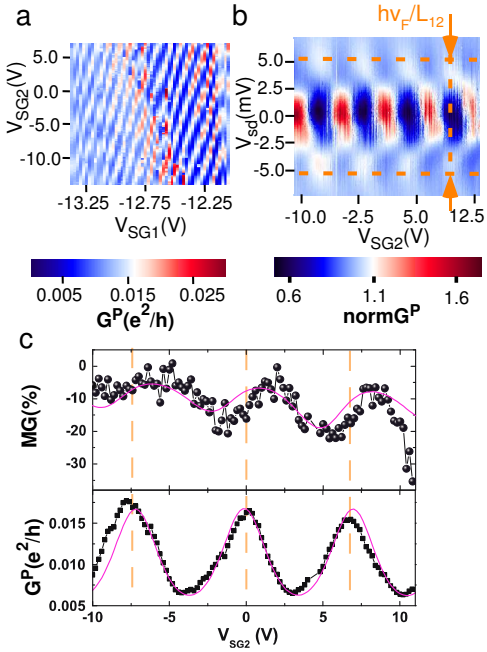


FIG. 6: **a.** Colorscale plot of G^P as a function of V_{SG1} and V_{SG2} for sample III. **b.** Colorscale plot of the normalized G of sample III as a function of V_{sd} and V_{SG2}. **c.** Simultaneous variations of MG and G^P as a function of V_{SG2} for sample III.

ior which is revealed by the complex switching features of both V_{34} and G in figure 5a and b. Because of their complexity, these features show that the hysteretic behaviors of V_{34} and G have strong correlations. As expected, we obtain more regular switchings if the magnetic field is applied *along* the easy axis anisotropy, as shown in figures 1b, 5c and 5d. As highlighted by the vertical dashed green lines, both the shape and the sign of the spin signals are again strongly correlated, which confirms that they have the same physical origin i.e. the change in the relative magnetic configuration of the two ferromagnetic contacts. Due to quantum interferences, MG naturally depends on V_{SG2} (see figure 5b and 5d)[27]. Therefore, we observe a spin field effect transistor action which is non-local with respect to the position of both the ferromagnetic electrodes and the gates. Note that in figure 5a and 5c, we observe a *negative* MV. This behavior is specific to the coherent regime and can be reproduced with the model of ref. 27.

The dependence of G and its hysteretic part $MG = 100(1 - G^{AP}/G^P)$ on the side gate voltages further reveals how the spin signals are affected by non-local quantum interferences. Figure 6a displays the colorscale plot of G as a function of V_{SG1} and V_{SG2} for sample III. As indicated by the tilted red stripes, interference fringes are observed in the conductance. The modulations in G are controlled essentially by a single winding phase, namely δ_{12}, which can be tuned via V_{SG2} or V_{SG1}. As shown in figure 6b, the colorscale plot of the normalized G as a function of V_{sd} and V_{SG2} displays the characteristic Fabry-Perot pattern with a level spacing of about $5meV$, consistent with the lithographically defined length L_{12} of about $300nm$ and a Fermi velocity of $8 \times 10^5 m/s$. The simultaneous measurement of G and MG as a function of V_{SG2} is shown in figure 6c. Here, we have measured MG versus V_{SG2} by recording a full hysteresis cycle for each set of gate voltages. As shown on the bottom panel, G^P oscillates from 0.008 to $0.017 \times e^2/h$ when V_{SG2} is swept. Oscillations of about 30% are also found in MG. The solid magenta lines correspond to the result of the scattering theory at $T = 4.2K$. We find a very good agreement with our experimental findings. From the theoretical fit of figure 6c, we conclude that MG varies due to changes in δ_{34} but also δ_{23} and δ_{12}. First, the gate electrode 2, which is nearby section 34 of the device, also acts on δ_{12} and δ_{23} thanks to the long range nature of Coulomb interaction (an effect described e.g. by $\beta_{12} \neq 0$ in the appendix). Second, the MG signal is also affected by V_{SG2} due to the spatial extension of the carriers wave function over the whole device. The non-local transistor-like action shown in figure 6c is therefore non-local electrostatically and quantum mechanically. Importantly, in figure 6c, the position of the maxima in G^P do not coincide with those of MG as highlighted by the vertical orange dashed lines. This reveals that G^{AP} oscillates in a similar fashion as G^P but with a *different phase*. The phase shift between G^P and G^{AP} clearly illustrates that the phase of the carriers is conserved upon scattering be-

low the ferromagnetic contact 2. Indeed, this effect can only be explained by invoking coherent electronic wave functions which extend from contact 1 to 3 at least, and give rise to spin-dependent resonance effects sensitive to the magnetic configuration of both leads 2 and 3. The theoretical curve of figure 6c reproduces accurately this effect. We conclude that, in our devices, both the spin and the orbital phase are conserved over the whole active part of the nanotube, *even below the ferromagnetic contacts*.

VI. CONCLUSION

In this work, we have studied various non-local transport phenomena in single wall carbon nanotubes connnected to two ferromagnetic and two normal electrodes. These multiterminal spintronics devices exploit actively both the spin and the orbital phase degrees of freedom on the same footing, in spite of the use of ferromagnetic elements. These findings could have interesting implications for the manipulation of the electronic spin in nanoscale conductors.

VII. APPENDIX : MODELING OF OUR DEVICES

Throughout the paper, we use the theory of reference 27 to explain our experimental findings. Each of our device is characterized by the set $\{T_{1K}, T_{1K'}, T_2, P_2, \varphi_2^R, \Delta\varphi_2^R, \varphi_2^T, \Delta\varphi_2^T, T_3, P_3, \varphi_3^R, \Delta\varphi_3^R, \varphi_3^T, \Delta\varphi_3^T, T_{4K}, T_{4K'}, C_{Q12}, C_{Q23}, C_{Q34}\}$, where $T_{1(4)K[K']}$ is the transmission probability from the normal electrode 1(4) to the nanotube for the K[K'] orbital, $T_{2(3)}$ is the transmission probability between the two nanotube sections adjacent to contact 2(3), $P_{2(3)}$ is the corresponding tunnel spin polarization, $\varphi_{2,(3)}^{T[R]}$ is the spin averaged scattering phase for an electron transmission below the contact 2(3) [an electron reflection against 2(3)], and $\Delta\varphi_{2,(3)}^R, \Delta\varphi_{2,(3)}^T$ are the Spin Dependence of Interfacial Phase Shifts (SDIPS) at contact 2(3) (see ref. 27). Due to the unitarity of the contact scattering matrices, the transmission from lead 2(3) to the nanotube is set by the above parameters. The results of the scattering theory at $T = 4.2K$ shown in magenta correspond to the set $\{0.25, 0.85, 0.002, 0.4, \pi, 0, 0, 0, 0.45, 0.4, \pi, 0, 0, 0, 0.29, 0.9, 11, 2.2, 18.0\}$ in figure 3c and to the set $\{0.89, 0.89, 0.000035, 0.8, \pi, 0.3\pi, 0.295\pi, 0.7\pi, 0.3, 0.8, \pi, 0.3\pi, 0.175\pi, 0, 0.95, 0.95, 31, 0.12, 5.0\}$ in figure 6c. The capacitances are in aF units. For the second case, contrarily to the case of sample I, we had to include a finite SDIPS at the ferromagnetic contacts to enhance the amplitude of the oscillations in MG[29,30].

We emphasize that the above parameters are subject to several constraints which minimize substantially the allowed phase space for our fitting procedure. The capacitances can be estimated from the resonance patterns in the G and V_{34} greyscale plots (see section V). The transmission probabilities can be estimated from the measurement of the two probe conductance of each section of the device at room temperature. The values of G, MG, V_{34} and MV measured at low temperature constraint further the transmission probabilities but also the scattering phases and the tunnel spin polarizations. Note that for sample III, we find a very small value of T_2 combined with a high value of $P_{2,3}$ and $\Delta\varphi_{2,(3)}^T$. These parameters are necessary to obtain the high MG and very low G^P observed in figure 6c. The observed zero bias anomaly in G is a possible signature of electron-electron interactions. This effect is compensated in figure 4b by normalizing G by its average V_{sd}-dependence over all the gate voltages presented in the figure.

To describe the influence of the gate voltages on the circuit, we introduce the relation $\delta_{ij} = \pi C_{Qij}(\alpha_{ij}V_{SG1} + \beta_{ij}V_{SG2})/e$, e being the elementary charge, $C_{Qij} = 2e^2L_{ij}/hv_F$ being the quantum capacitances of each nanotube section, the dimensionless couplings α_{ij} and β_{ij} being determined by the full electrostatic problem of our devices.

FIG. 7:
(Figure file too big-see published version for the figure) Electrostatic diagram of our devices. We assume here only nearest neighbor electrostatic coupling.

In determining the gate dependence of the theoretically expected signals, it is important to supplement the scattering theory with a self-consistent determination of the electrostatic potential of the circuit. We use a coarse-grained version of the Poisson equation which we solve self-consistently in order to determine the different side gate actions. Our calculation proceeds along the lines of ref.[33]. We start with the full electrostatic matrix capacitance of our devices which can be derived from the electrostatic diagram of figure 7. We use a nearest neighbor scheme. The total capacitance matrix C_{TOT} reads :

$$C_{TOT} = \begin{pmatrix} C_L & 0 & 0 & 0 & 0 & 0 & -C_L & 0 & 0 \\ 0 & C_R & 0 & 0 & 0 & 0 & 0 & 0 & -C_R \\ 0 & 0 & 2C_{F_L} & 0 & 0 & 0 & -C_{F_L} & -C_{F_L} & 0 \\ 0 & 0 & 0 & 2C_{F_R} & 0 & 0 & 0 & -C_{F_R} & -C_{F_R} \\ 0 & 0 & 0 & 0 & C_{G_1} & 0 & -C_{G_1} & 0 & 0 \\ 0 & 0 & 0 & 0 & 0 & C_{G_2} & 0 & 0 & -C_{G_2} \\ -C_L & 0 & -C_{F_L} & 0 & -C_{G_1} & 0 & C_{\Sigma_1} & -C_{m_1} & 0 \\ 0 & 0 & -C_{F_L} & -C_{F_R} & 0 & 0 & -C_{m_1} & C_{\Sigma_2} & -C_{m_2} \\ 0 & -C_R & 0 & -C_{F_R} & 0 & -C_{G_2} & 0 & -C_{m_2} & C_{\Sigma_3} \end{pmatrix} \quad (1)$$

with $C_{\Sigma_1} = C_L + C_{F_L} + C_{m_1} + C_{G_1}, C_{\Sigma_2} = C_{m_1} + C_{F_R} + C_{F_L} + C_{m_2}, C_{\Sigma_3} = C_R + C_{F_R} + C_{m_2} + C_{G_2}$

In principle, we should determine self-consistently the electrostatic potentials on each section of the nanotube using the full scattering matrix of the problem. This would go beyond the scope of this work. For the sake of simplicity, we assign a constant value for the electrochemical capacitance of each section. This assumption is reasonable in our case because the high coupling of the SWNT to the normal electrodes reduces the energy dependence of the electrochemical capacitance. The self-consistent equation for the electrostatic potential of each NT section reads :

$$\begin{cases} (C_{\Sigma_1} + 2C_{Q_{12}})\delta U_{NT12} - C_{m1}\delta U_{NT23} = C_{G_1}\delta V_{SG1} \\ -C_{m1}\delta U_{NT12} + (C_{\Sigma_2} + 2C_{Q_{23}})\delta U_{NT23} - C_{m2}\delta U_{NT34} = 0 \\ -C_{m2}\delta U_{NT23} + (C_{\Sigma_3} + 2C_{Q_{34}})\delta U_{NT34} = C_{G_2}\delta V_{SG2} \end{cases} \quad (2)$$

Finally, we get,

$$\begin{pmatrix} \alpha_{12} & \beta_{12} \\ \alpha_{23} & \beta_{23} \\ \alpha_{34} & \beta_{34} \end{pmatrix} = \begin{pmatrix} \frac{(C_{\mu_2}C_{\mu_3} - C_{m_2}^2)C_{G1}}{C_{\mu_1}C_{\mu_2}C_{\mu_3} - C_{\mu_3}C_{m_1}^2 - C_{\mu_1}C_{m_2}^2} & \frac{C_{m_1}C_{m_2}C_{G2}}{C_{\mu_1}C_{\mu_2}C_{\mu_3} - C_{\mu_3}C_{m_1}^2 - C_{\mu_1}C_{m_2}^2} \\ \frac{C_{\mu_3}C_{m_1}C_{G1}}{C_{\mu_1}C_{\mu_2}C_{\mu_3} - C_{\mu_3}C_{m_1}^2 - C_{\mu_1}C_{m_2}^2} & \frac{C_{\mu_1}C_{m_2}C_{G2}}{C_{\mu_1}C_{\mu_2}C_{\mu_3} - C_{\mu_3}C_{m_1}^2 - C_{\mu_1}C_{m_2}^2} \\ \frac{C_{m_1}C_{m_2}C_{G1}}{C_{\mu_1}C_{\mu_2}C_{\mu_3} - C_{\mu_3}C_{m_1}^2 - C_{\mu_1}C_{m_2}^2} & \frac{(C_{\mu_2}C_{\mu_1} - C_{m_2}^2)C_{G2}}{C_{\mu_1}C_{\mu_2}C_{\mu_3} - C_{\mu_3}C_{m_1}^2 - C_{\mu_1}C_{m_2}^2} \end{pmatrix} \quad (3)$$

For a realistic set of capacitances $\{C_L, C_{F_L}, C_R, C_{F_R}, C_{m_1}, C_{m_2}, C_{G1}, C_{G2}, C_{Q12}, C_{Q23}, C_{Q34}\}$ of about $\{10aF, 10aF, 10aF, 10aF, 100aF, 100aF, 1aF, 1aF, 30aF, 1aF, 10aF\}$, we find $\alpha's$ and $\beta's$ which are in good agreement with the observed slopes in the different tartan patterns. For example, for the above parameters, we get the following coupling matrix :

$$\begin{pmatrix} 0.00837 & 0.00311 \\ 0.00441 & 0.00502 \\ 0.00328 & 0.01131 \end{pmatrix} \quad (4)$$

For each fitting procedure, one has to adjust the values of the $\alpha's$ and the $\beta's$ in order to account for the gate dependence of the observed signals. We use values which are consistent with the above determination. Note that we have omitted the influence of the back gate voltage here since it is set to a constant value in our measurements.

Acknowledgments

We are indebted with M. Aprili for discussions and sharing his thin film deposition equipment at the beginning of this work and with A. Thiaville, S. Rohart and J.-Y. Chauleau for illuminating discussions on the micromagnetics of the NiPd and for MFM characterization of our ferromagnetic contacts. The devices have been made within the consortium Salle Blanche Paris Centre. This work is supported by the EU contract FP6-IST-021285-2 and by the CNano Ile de France contract SPINMOL.

[1] M. N. Baibich, J.M. Broto, A. Fert et al., Phys. Rev. Lett. **61**, 2472 (1988).
[2] G. Binasch, P. Grünberg, F. Saurenbach and W. Zinn, Phys. Rev. B **39**, 4828 (1989).
[3] I. Zutic, J. Fabian and S. Das Sarma, Rev. Mod. Phys. **76**, 323 (2004).
[4] A. Pasupathy, R.C. Bialczak, J. Martinek *et al.* Science **306**, 86 (2004).

[5] S. Sahoo, T. Kontos, J. Furer et al. Nature Phys. **1**, 99 (2005).
[6] H.T. Man, I.J.W. Wever and A.F. Morpurgo Phys. Rev. B **73**, 241401(R) (2006).
[7] J.R. Hauptmann, J. Paaske, P.E. Lindelof Nature Phys. **4**, 373 (2008).
[8] L.E. Hueso, J.M. Pruneda, V. Ferrari et al. Nature **445**, 410 (2007).
[9] A. Cottet, T. Kontos, S. Sahoo et al. Semicond. Sci. and Technol. **21**, S78 (2006).
[10] G. Gunnarsson, J. Trbovic, C. Schönenberger Phys. Rev. B **77**, 201405(R) (2008).
[11] N. Tombros, S.J. van der Molen and B.J. van Wees Phys. Rev. B **73**, 233403 (2006).
[12] A. Brataas, Yu. V. Nazarov and G.E.W. Bauer Phys. Rev. Lett. **84**, 2481 (2000).
[13] D. Huertas-Hernando, Yu.V. Nazarov and W. Belzig Phys. Rev. Lett. **88**, 047003 (2002).
[14] A. Cottet, W. Belzig and C. Bruder Phys. Rev. Lett. **92**, 206801 (2004).
[15] I. Adagideli, G.E.W. Bauer and B.I. Halperin Phys. Rev. Lett. **97**, 256601 (2006).
[16] D. Urban, M. Braun and J. König Phys. Rev. B **76**, 125306 (2007).
[17] C.P. Umbach, P. Santhanam, C. van Haesendonck and R.A. Webb Appl. Phys. Lett. **50**, 1289 (1987).
[18] M. Büttiker Phys. Rev. Lett. **57**, 1761 (1986).
[19] A. Makarovski, A. Zhukov,J. Liu and G. Finkelstein Phys. Rev. B **76**, 161405(R) (2007).
[20] M. Johnson and R.H. Silsbee Phys. Rev. Lett. **55**, 1790 (1985).
[21] X. Lou, C. Adelmann, S.A. Crooker *et al.* Nature Phys. **3**, 197 (2007).
[22] M. Zaffalon and B.J. van Wees Phys. Rev. B **71**, 125401 (2005).
[23] N. Tombros, C. Jozsa, M. Popinciuc *et al.* Nature **448**, 571 (2007).
[24] T. Valet and A. Fert Phys. Rev. B **48**, 7099 (1993).
[25] L. Vila, R. Giraud et al. Phys. Rev. Lett. **98**, 027204 (2007).
[26] F.J. Jedema, A.T. Filip and B.J. van Wees Nature **410**, 345 (2001).
[27] A. Cottet, C. Feuillet-Palma and T. Kontos Phys. Rev. B **79**, 125422 (2009).
[28] W.G. van der Wiel *et al.* Rev. of Mod. Phys. **75**, 1 (2003).
[29] A. Cottet, T. Kontos, W. Belzig *et al.* Europhys. Lett. **74**, 320 (2006).
[30] A. Cottet and M.-S. Choi, Phys. Rev. B, **74**, 235316 (2006).
[31] F. Kuemmeth, S. Ilani, D. C. Ralph and P. L. McEuen Nature **452**, 448 (2008).
[32] S. Takahashi and S. Maekawa Phys. Rev. B **67**, 052409 (2003).
[33] M. Büttiker and T. Christen "Mesoscopic electron transport" edited by L. Kowenhoven, G. Schoen and L. Sohn, NATO ASI Series E.